Materials Advances

ROYAL SOCIETY OF CHEMISTRY

PAPER

View Article Online
View Journal | View Issue

Cite this: *Mater. Adv.*, 2026, 7, 4880

Hyaluronic acid-modified Se@PDA@CDDP nanoplatform for synergistic chemo-photothermal therapy and immune activation *via* redox modulation

Yong Huang,†[a] Hong Hong,†[a] Lan Xia,[a] Lifang Huang,[a] Chuqi Shao,[a] Manli Qu,[a] Wenjun He,[a] Suqiong Liang,[a] Cunchuan Wang *[b] and Yanping Qiu*[c]

Immunosuppressive and redox-buffered tumor microenvironments limit cisplatin efficacy in colorectal cancer (CRC) and blunt antitumor immunity. Herein, we engineer a hyaluronic-acid-modified, pH/redox/NIR-responsive nanoplatform (Se@PDA@HA@CDDP) by the *in situ* growth of selenium on polydopamine, followed by cisplatin loading and HA cloaking for CD44-mediated targeting. The nanoparticles exhibit uniform size distribution, robust colloidal stability, strong light-to-heat conversion, and GSH-consuming/ROS-amplifying activity, enabling on-demand drug release under acidic and GSH-rich conditions and NIR irradiation. *In vitro*, HA functionalization enhances cellular uptake and yields potent, NIR-augmented cytotoxicity characterized by mitochondrial depolarization (JC-1), apoptosis (Annexin V/PI), ROS burst (DCFH-DA), and GSH depletion while sparing normal cells. Mechanistically, Se@PDA@HA@CDDP treatment induces immunogenic cell death (ICD), as evidenced by calreticulin exposure and HMGB1 release, and concurrently activates NF-κB signaling (p-p65 upregulation). These events collectively promote macrophage polarization toward a pro-inflammatory M1 phenotype, accompanied by increased TNF-α and IL-6 secretion. *In vivo* imaging confirms HA-mediated tumor accumulation and superior photothermal performance; therapeutically, Se@PDA@HA@CDDP + NIR suppresses tumor growth, reduces angiogenesis (CD31) and proliferation (Ki67), and elevates apoptosis (TUNEL), alongside enhanced dendritic-cell maturation and intratumoral/lymph-node $CD3^+/CD8^+/CD4^+$ T-cell infiltration. Histology and serum biochemistry reveal no overt organ damage or hepatic/renal dysfunction, supporting favorable biosafety. These findings establish Se@PDA@HA@CDDP as a mechanism-guided platform that couples targeted chemotherapy with photothermal and immune activation for efficient and safe CRC therapy.

Received 25th November 2025,
Accepted 30th January 2026

DOI: 10.1039/d5ma01372k

rsc.li/materials-advances

1. Introduction

Colorectal cancer (CRC) remains one of the most prevalent and lethal malignancies worldwide, characterized by high recurrence rates and resistance to conventional chemotherapy.[1] Although platinum drugs such as cisplatin (CDDP) are cornerstones of systemic therapy, their efficacy in solid tumors is constrained by poor tumor selectivity, rapid off-target exposure, dose-limiting toxicities (notably nephro- and hepatotoxicity), and acquired resistance.[2] These clinical hurdles are compounded by an immunosuppressive, redox-buffered tumor microenvironment (TME), where intracellular glutathione (GSH) is abundant, ROS are efficiently scavenged, and hypoxia blunts oxidative injury, which, together, dampen DNA damage-induced apoptosis and limit the development of durable, immune-supported responses.[3,4]

Rational nanomedicine design aims to address these barriers simultaneously through the following strategies: (i) enriching drugs at tumors *via* passive and receptor-mediated targeting; (ii) gated release in response to tumor-like triggers (acidic pH and high GSH); (iii) reprograming redox homeostasis to amplify oxidative damage; and (iv) coupling local tumor debulking with systemic immune activation.[5,6] Selenium (Se) nanomaterials provide a distinctive redox lever. By engaging intracellular thiols, Se can form reactive selenide intermediates that consume GSH and amplify ROS, tipping cells toward oxidative stress and promoting inflammatory signaling.[7] Nevertheless, bare Se nanoparticles tend to aggregate and lose function in biological media,

[a] *The Sixth Affiliated Hospital of Jinan University (Dongguan Eastern Central Hospital), Dongguan, Guangdong, 523573, China*
[b] *The First Affiliated Hospital of Jinan University, Guangzhou, 510000, China. E-mail: twcc@jnu.edu.cn*
[c] *The Fifth Affiliated Hospital of Jinan University (Heyuan Shenhe People's Hospital), Heyuan, Guangdong, 517000, China. E-mail: quick504@163.com*
† These authors contributed equally to the present research.

necessitating stabilizing scaffolds that also allow co-delivery of therapeutics and on-demand activation.[8]

Polydopamine (PDA) offers such a multifunctional framework. It nucleates and stabilizes Se grown *in situ*, presents catechol/amine chemistry for drug coordination or adsorption, and efficiently converts near-infrared (NIR) light into heat, enabling spatiotemporally controlled, synergistic chemo-photothermal therapy (PTT).[9–11] Hyaluronic acid (HA), a natural ligand for CD44 receptors overexpressed on many tumor cells, further provides active targeting and prolonged tumor retention while improving blood compatibility and colloidal stability.[12–14] Integrating Se, PDA, and HA within a single construct creates the opportunity to combine (i) CD44-mediated uptake, (ii) pH/GSH-triggered payload release, (iii) selenium-driven GSH depletion/ROS amplification, and (iv) NIR-boosted cytotoxicity within the same delivery vehicle.[15]

Beyond direct cytotoxicity, next-generation nanotherapeutics are increasingly evaluated by their ability to reshape antitumor immunity. Immunogenic cell death (ICD)-marked by calreticulin (CRT) exposure and HMGB1 release-can enhance antigen presentation and prime T-cell responses.[16–18] At the innate interface, NF-κB-linked signaling pathways steer macrophage phenotypes, foster dendritic-cell maturation, and support cytotoxic T-cell infiltration.[19,20] Materials that simultaneously heighten oxidative stress, expose ICD hallmarks, and engage these immune axes hold particular promise for bridging local tumor control with systemic antitumor immunity.[21,22]

Herein, we have engineered a hyaluronic-acid-modified, pH/redox/NIR-responsive nanoplatform (Se@PDA@HA@CDDP) by the *in situ* growth of Se on PDA, followed by CDDP loading and HA cloaking (Scheme 1). The design rationale is fourfold: (1) HA endows CD44-mediated internalization and tumor accumulation; (2) acidic/GSH-rich niches promote Se/CDDP release and selenium-driven redox cycling; (3) NIR irradiation augments drug release and local hyperthermia to heighten damage; and (4) combined redox stress and thermal/chemotherapeutic injury elicit ICD and activate NF-κB–dependent macrophage repolarization.[23] We hypothesize that this integrated mechanism will couple precise delivery and controlled release with redox reprogramming and immune activation, thereby overcoming canonical barriers to CDDP in CRC. Unlike existing PDA@HA@CDDP systems, which focus primarily on drug delivery and basic photothermal therapy, our platform further integrates redox modulation and immune activation to not only enhance tumor cell killing but also stimulate immune responses, offering a promising dual therapeutic strategy.

We validate this concept through comprehensive physicochemical characterization and functional assays. *In vitro*, we assess HA-mediated uptake, cytotoxicity with NIR augmentation, mitochondrial depolarization, apoptosis, ROS surge, and GSH depletion; we further interrogate ICD hallmarks (CRT, HMGB1) and NF-κB activation, along with macrophage polarization and cytokine profiles. *In vivo*, fluorescence/thermal imaging defines biodistribution and photothermal behavior, while therapeutic studies in MC38 tumors quantify tumor growth inhibition, angiogenesis (CD31), cell proliferation (Ki67), and apoptosis (TUNEL), accompanied by dendritic-cell maturation and intratumoral/lymph-node T-cell responses ($CD3^+$, $CD8^+$, and $CD4^+$). Biosafety is examined by organ histology and serum biochemistry. Together, these investigations position selenium-driven redox

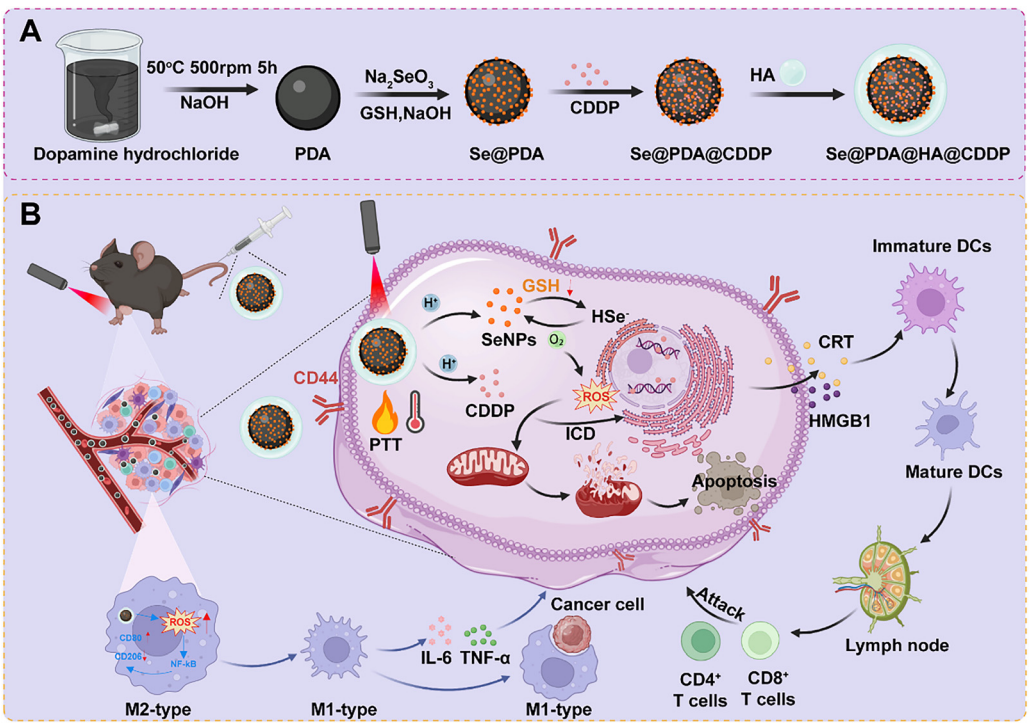

Scheme 1 Schematic of the synthesis (A) and therapeutic mechanism (B) of Se@PDA@HA@CDDP.

modulation within an HA-targeted, PDA-enabled architecture as a unifying strategy to synergize cisplatin chemotherapy with photothermal and immune activation for effective and safe CRC treatment.

2. Materials and methods

2.1. Preparation of PDA

Dopamine hydrochloride (180 mg) was introduced into 90 mL of deionized water and allowed to fully dissolve under vigorous magnetic stirring. After a clear solution was obtained, 0.8 mL of freshly prepared 1 M NaOH was slowly dripped into the flask. The mixture was then kept at 50 °C with continuous stirring for 5 h to trigger the oxidative self-polymerization of dopamine. At the end of the reaction, the dispersion was transferred into a dialysis bag (molecular weight cut-off 3500 Da) and dialyzed against excess deionized water to remove low-molecular-weight impurities. The retained fraction was frozen and lyophilized to yield PDA powder.

2.2. Preparation of Se@PDA

Na_2SeO_3 (10.72 mg) and GSH (49.2 mg) were first completely solubilized in deionized water to obtain a transparent solution, into which PDA powder (40 mg) was subsequently added and dispersed. Afterwards, 800 μL of 0.2 M NaOH was gradually introduced under stirring, and the reaction was allowed to proceed for 2 h. The generated Se@PDA particles were harvested by centrifugation, and the pellets were rinsed several times with deionized water to remove unreacted species.

2.3. Preparation of Se@PDA@CDDP

For CDDP loading, Se@PDA (2 mg) was suspended in 5 mL of deionized water and vortexed or mildly sonicated until a uniform dispersion was formed. Then, 1 mL of a CDDP solution in DMSO (containing 2 mg CDDP) was added dropwise under gentle stirring. The dispersion was maintained at room temperature under stirring overnight to allow sufficient adsorption of CDDP onto the Se@PDA surface. Nanoparticles were then separated by centrifugation (8000 rpm, 10 min), the resulting pellets were washed twice with deionized water to remove free drug, and the solid was dried to obtain Se@PDA@CDDP.

2.4. Preparation of Se@PDA@HA@CDDP

Se@PDA@CDDP (2 mg) was mixed with 5 mL of a sodium hyaluronate solution (1%, molecular weight 150–250 kDa), and the mixture was gently stirred at 4 °C for 48 h to allow HA adsorption onto the nanoparticle surface. Subsequently, the suspension was centrifuged, and the pellets were washed three times with deionized water. The final product, denoted as Se@PDA@HA@CDDP, was collected as HA-coated nanoparticles.

2.5. Characterization

The morphology and elemental distribution of the nanoparticles were observed using a high-resolution transmission electron microscope (H-800, Hitachi, Japan) operated at 200 kV and equipped with an energy-dispersive X-ray spectroscopy (EDS) system for mapping C, O and Se. The hydrodynamic size distribution and zeta potential at 25 °C were determined on a Zetasizer Nano ZS90 analyzer (Malvern). Fourier-transform infrared (FTIR) spectra were collected on a Vertex 70 spectrometer (Bruker) in the 4000–400 cm^{-1} region with KBr pellets. Ultraviolet-visible (UV-Vis) absorption spectra were recorded on a V-3100PC spectrophotometer over the wavelength range of 200–800 nm. Surface composition and valence states were characterized by X-ray photoelectron spectroscopy (XPS, Thermo ESCALAB 250Xi) operated with Al Kα radiation ($h\nu$ = 1486.6 eV), and the binding energy scale was referenced to the C 1s peak at 284.8 eV. The photothermal behavior of the nanoparticles under 808 nm irradiation was evaluated with a continuous-wave laser (Changchun Leilui Optoelectronic Technology Co., Ltd.), and the temperature increase was monitored by an E60 infrared thermal camera (FLIR).

2.6. Drug release of Se@PDA@HA@CDDP

The *in vitro* release from Se@PDA@HA@CDDP was evaluated by a dialysis method. Briefly, 1 mL of the nanoparticle dispersion was loaded into a dialysis membrane with a molecular weight cut-off of 1000 Da, sealed, and then transferred into a 15 mL centrifuge tube containing 2 mL of release buffer. Media with different environments were employed (pH 7.4, pH 6.0, pH 6.0 + NIR, pH 6.0 + GSH (10 mM), and pH 6.0 + GSH (10 mM) + NIR). The tubes were mounted on a shaker operating at 150 rpm. At scheduled sampling points, 1 mL of the outer solution was taken for analysis, after which the same volume of fresh PBS was added back so that the total volume of the release phase remained unchanged. For the NIR-responsive groups, the samples were irradiated with an 808 nm near-infrared laser (1.5 W cm^{-2}) for 5 min immediately before each withdrawal. After 72 h of incubation, the concentration of liberated CDDP in the collected fractions was analyzed using a UV-vis spectrophotometer, and the cumulative release of selenium ions was calculated from Se contents determined by inductively coupled plasma optical emission spectrometry (ICP-OES).

2.7. Reactive oxygen species (ROS) assay

A panel of PBS solutions containing 0, 1, 2, 5, and 10 mM GSH was first prepared. Each solution was supplemented with methylene blue (MB, 10 μg mL^{-1}) and H_2O_2 (10 mM) and briefly vortexed to obtain a uniform blue reaction system. Subsequently, Se@PDA was introduced to a final concentration of 200 μg mL^{-1}. The decay of MB was followed *via* UV-vis spectra, tracking the characteristic band at 665 nm, which served as an indicator of ROS-mediated MB degradation. All assays were carried out at room temperature with at least three parallel samples for each GSH concentration.

2.8. GSH depletion assay

To evaluate the GSH-consuming capacity of Se@PDA, nanoparticle dispersions (200 μg mL^{-1}) were incubated with 5 mM GSH in PBS. Aliquots were withdrawn at predefined time points (0, 0.5, 1, 3, 5, 7, and 24 h). Each aliquot was immediately

reacted with Ellman's reagent (DTNB) so that the DTNB concentration in the mixture reached 0.2×10^{-3} M. DTNB reacts stoichiometrically with free thiol groups to generate the yellow chromophore TNB. After completion of the color development, UV-vis spectra were recorded and the intensity of the TNB band at 412 nm was used to calculate the remaining GSH level. A gradual reduction of this signal reflected the extent of GSH depletion caused by Se@PDA.

2.9. Cytotoxicity assay

L929 cells were distributed into 96-well plates at 5×10^4 cells per mL (100 μL per well) and allowed to establish a monolayer during the initial 24 h of culture. After stabilization, the culture medium was exchanged for fresh medium containing graded concentrations of Se@PDA@HA@CDDP (0–800 μg mL^{-1}). Following an additional 24 h of exposure, the medium in each well was discarded and replaced with CCK-8 working solution. Color development proceeded under standard culture conditions, after which the optical density at 450 nm was read on a microplate spectrometer. The cell viability was calculated using the following equation:[24]

$$\text{Cell viability}\,(\%) = \frac{A_s - A_b}{A_0 - A_b} \times 100$$

where A_s is the absorbance of the sample, A_b is the blank absorbance, and A_0 is the absorbance of the control group.

The same workflow was adopted for MC38 cells, which were plated at an identical density and allowed to acclimate for 24 h prior to drug exposure. After treatment with serial dilutions of the formulations for another 24 h, metabolic activity was quantified by introducing the CCK-8 solution and subsequently determining the OD_{450} signal. Cytotoxicity toward MC38 cells was calculated using the above equation.

2.10. Live-dead cell staining

The damage of the drug to MC38 cells was further observed through live/dead cell staining experiments. MC38 cells (8×10^4 cells per mL) were seeded in 12-well plates with 1 mL of culture medium per well and cultured overnight until a stable adherent cell layer formed. The cells were then incubated with different formulations (control, Se@PDA@HA, Se@PDA@HA@CDDP, Se@PDA@HA@CDDP, concentrations of 100 μg mL^{-1}), and after 6 h, some wells were irradiated with a laser (808 nm, 1.5 W cm^{-2}, 5 min). After 24 h of culture, the supernatant was discarded, and the cells were washed once with PBS buffer. Then, a mixture of Calcein-AM and propidium iodide (PI) staining solution diluted with PBS (prepared according to the kit instructions) was added. Staining was performed at 37 °C in the dark for 30 min, followed by gentle washing with PBS buffer to remove excess dye. The green fluorescence of Calcein-AM (live cells) and the red fluorescence of PI (dead cells) were captured using a fluorescence microscope, and the representative microscopic fields of view for each group were recorded to compare the ratio of live to dead cells.

2.11. Wound-healing (scratch) assay

The influence of the formulations on MC38 cell motility was assessed by a scratch assay. MC38 cells were grown in 12-well plates until a continuous monolayer was obtained. A straight gap was then drawn across the monolayer with a sterile 200-μL pipette tip. Detached cells were eliminated by two gentle PBS rinses, and low-serum medium (1% FBS) containing the indicated drugs (control, Se@PDA@HA, Se@PDA@HA@CDDP, and Se@PDA@HA@CDDP concentration of 100 μg mL^{-1}) was added to each well; some wells were irradiated with a laser (808 nm, 1.5 W cm^{-2}, 5 min). Plates were returned to a 37 °C, 5% CO_2 incubator. Phase-contrast images of the same scratched region were taken immediately after scratching (defined as 0 h) and again after 24 h. The scratch area at each time point was outlined in ImageJ software, and the percentage of migration was calculated as follows:

$$\text{Cell migration rate}\,(\%) = \frac{T_0 - T}{T_0} \times 100$$

where T_0 represents the scratch area immediately after scratching (0 h), and T represents the scratch area after 24 h of treatment.

2.12. Apoptosis assay

The programmed cell death of MC38 cells under different treatments was quantified by a flow-cytometric apoptosis assay. Briefly, MC38 cells were inoculated into 12-well plates at 8×10^4 cells per mL (1 mL per well) and cultured overnight to form a stable adherent layer. The culture medium was then replaced with fresh medium containing the indicated drug formulations (control, Se@PDA@HA, Se@PDA@HA@CDDP, Se@PDA@HA@CDDP at concentrations of 100 μg mL^{-1}). Cells were divided into six treatment groups: control, Se@PDA@HA and Se@PDA@HA@CDDP, each with or without 808 nm NIR laser irradiation (1.5 W cm^{-2}, 5 min). For the irradiation groups, laser exposure was applied at the end of the 24 h drug incubation. At the end of the exposure period, cultures were rinsed with PBS, detached with trypsin, and collected by gentle centrifugation. The resulting cell pellets were resuspended in binding buffer from a commercial apoptosis detection kit and incubated with the kit staining solution in the dark for the time specified in the protocol. Stained samples were immediately subjected to flow-cytometric acquisition, and the percentage of apoptotic cells in each group was calculated from the corresponding fluorescence dot plots.

2.13. Cellular uptake assay

Cellular internalization of Se@PDA and Se@PDA@HA was examined with ICG-labeled nanoparticles. Se@PDA and Se@PDA@HA were first conjugated with ICG to obtain fluorescent probes. MC38 cells were distributed into 12-well plates (8×10^4 cells per mL, 1 mL per well) and grown overnight until a uniform adherent layer was formed. The culture medium was then exchanged for fresh medium containing either Se@PDA@ICG or Se@PDA@HA@ICG (100 μg mL^{-1}), and the cells

were exposed for 1, 2, 4, or 6 h. At each time point, the cells were rinsed with PBS, detached, collected by gentle centrifugation and resuspended in PBS for flow-cytometric analysis. ICG fluorescence of the cell population was recorded, and mean fluorescence intensity (MFI) values were obtained from FlowJo software to compare the uptake behavior of Se@PDA and Se@PDA@HA.

2.14. ROS generation assay

Intracellular ROS in MC38 cells were monitored using the DCFH-DA probe. MC38 cells were plated in 12-well plates at 8×10^4 cells per mL and allowed to attach overnight, after which the medium was replaced with fresh medium containing the designated formulations (control, Se@PDA@HA, Se@PDA@HA@CDDP, and Se@PDA@HA@ CDDP concentration of 100 μg mL^{-1}); after 6 h, some wells were irradiated with a laser (808 nm, 1.5 W cm^{-2}, 5 min). Following a 24 h treatment period, supernatants were discarded and the cells were washed once with PBS. A DCFH-DA working solution prepared in PBS (according to the probe instructions) was then added, and the plates were kept at 37 °C in the dark for 30 min to load the probe. After incubation, excess dye was removed by washing with PBS. The green fluorescence originating from oxidized DCF was captured using a fluorescence microscope. For semi-quantitative analysis, images from representative fields were processed in ImageJ, and the mean fluorescence intensity of each group was used as an indicator of intracellular ROS levels.

2.15. Mitochondrial membrane potential disruption assay

Mitochondrial membrane potential ($\Delta\Psi_m$) changes in MC38 cells were examined using the JC-1 dye. MC38 cells were distributed into 12-well plates (8×10^4 cells per mL, 1 mL per well) and maintained overnight to allow the formation of a uniform adherent layer. Thereafter, wells were supplied with the corresponding formulations (control, Se@PDA@HA, Se@PDA@HA@CDDP, and Se@PDA@HA@ CDDP at a concentration of 100 μg mL^{-1}) and after 6 h, some wells were irradiated with a laser (808 nm, 1.5 W cm^{-2}, 5 min). The cultures were kept under standard incubation conditions for 24 h. Following exposure, the supernatant was discarded and residual medium was removed by a gentle PBS rinse. A JC-1 working solution prepared in PBS was then added, and the plates were protected from light for 30 min at 37 °C to facilitate probe loading. After staining, the cells were washed once with PBS, and images of JC-1 red (aggregates) and green (monomers) fluorescence were captured using a fluorescence microscope. The ratio of green to red fluorescence, reflecting $\Delta\Psi_m$ disruption, was quantified through ImageJ analysis.

2.16. Macrophage polarization assay

Flow cytometry was used to evaluate Se@PDA@HA@CDDP-induced macrophage polarization. Cells were seeded at a density of 8×10^4/mL in 12-well plates. After cell attachment, different drug groups were added to each well (control, Se@PDA@HA, Se@PDA@HA@CDDP, and Se@PDA@HA@ CDDP at a concentration of 100 μg mL^{-1}) and after 6 h, some wells were irradiated with a laser (808 nm, 1.5 W cm^{-2}, 5 min). After incubation in a cell culture incubator for 24 hours, the cells were harvested. The harvested cells were washed twice with PBS and blocked with 1% BSA. The cells were then stained according to the kit instructions in the dark. Finally, apoptotic events were quantified by flow cytometry.

2.17. Animals and tumor model establishment

Specific-pathogen-free (SPF) female C57BL/6 mice (5–6 weeks old) were obtained from Guangzhou Ruige Biotechnology Co., Ltd. After arrival, animals were kept in the institutional animal facility under standard housing conditions for a 10-day acclimation and health-monitoring period. Only mice showing normal physiological status were used for subsequent procedures. All animal experiments were performed in accordance with relevant national regulations and institutional guidelines for the care and use of laboratory animals, and were approved by the Institutional Animal Care and Use Committee (IACUC) of Zhuhai Baishitong Biotechnology Co., Ltd. For the construction of the MC38 tumor model, murine colon carcinoma MC38 cells were collected after trypsinization, pelleted by centrifugation, and re-suspended in PBS. The resulting cell suspension was blended 1 : 1 with high-concentration Matrigel. A total of 100 μL of this mixture, containing 1.5×10^6 MC38 cells, was delivered subcutaneously into the left axillary region of each mouse. Tumor growth was assessed daily, and therapeutic intervention began once the tumor volume reached approximately 100 mm^3.

2.18. *In vivo* antitumor activity studies

Once palpable tumors had formed, mice were allocated into five treatment groups ($n = 5$ per group): PBS, CDDP, Se@PDA@CDDP + NIR, Se@PDA@HA@CDDP, and Se@PDA@CDDP@HA + NIR. CDDP-containing formulations were administered at 5 mg kg^{-1}. All treatments were given every two days over a 21-day period. Throughout the study, tumor dimensions and body weight were recorded every two days. At the end of the 21-day treatment window, mice were sacrificed, and tumors were excised, weighed, and imaged to assess therapeutic efficacy.

2.19. *In vivo* fluorescence imaging and thermal imaging analysis

The tumor-targeting ability of Se@PDA@HA was evaluated using fluorescence imaging experiments conducted on mice using a small animal live imaging system. Two nude mice bearing tumors of approximately 100 mm^3 were selected. Then, 100 μL of the Se@PDA@ICG complex and the Se@PDA@HA@ICG complex (200 μg mL^{-1}) were injected *via* the tail vein. Fluorescence imaging of the nude mice was performed using a small animal live imaging system (FX Pro, Bruker) at various time intervals. Eight hours after injection, the mice were sacrificed, and their hearts, livers, spleens, lungs, kidneys, and tumor tissues were removed for *ex vivo* imaging. The excitation wavelength was 780 nm, and the emission wavelength was 810 nm.

In order to evaluate the *in vivo* thermal imaging effect of the material, when the mouse tumor grew to an appropriate size,

the tumor-bearing mice were injected with PBS, Se@PDA, and intratumoral injection of Se@PDA@HA, respectively. They were irradiated with an 808 nm laser with a power density of 1.5 W cm^{-2} for 5 minutes, photos were taken with an infrared thermal imager, and the temperature was recorded every 10 seconds.

2.20. Flow cytometric analysis

To characterize treatment-induced changes in anti-tumor immunity, lymph nodes were excised and processed into single-cell suspensions for multiparameter flow cytometry. Surface markers were detected using fluorophore-conjugated antibodies, including APC-anti-mouse CD3, PE/Cy7-anti-mouse CD8a, and FITC-anti-mouse CD4, enabling the separation of cytotoxic T cells (CTLs; $CD3^+CD4^-CD8^+$) from helper T cells ($CD3^+CD4^+CD8^-$). To identify dendritic cell subsets, cells were additionally labeled with APC-anti-mouse CD11c, FITC-anti-mouse CD80, and Precp-cy5.5-anti-mouse CD86. After staining, samples were washed, resuspended, and subjected to flow-cytometric acquisition. Populations were gated according to standard immunophenotyping strategies to determine immune-cell composition and activation states.

2.21. *In vivo* investigation of anti-tumor mechanisms

To dissect how each formulation influenced the tumor immune microenvironment and tissue remodeling, tumors were harvested on day 21 and processed for histological and immunofluorescence examinations. Paraffin-embedded sections were stained for CD3, CD4, CD8, Ki67, and CD31 to evaluate T-cell infiltration, proliferative activity, and neovascularization. Apoptotic cells were visualized using the TUNEL assay, while hematoxylin and eosin staining provided an overview of tissue structure, necrosis, and treatment-induced pathological changes. Images were captured under fluorescence or bright-field microscopy. Quantitative analysis of fluorescence and structural features was performed using ImageJ to obtain semi-quantitative comparisons among treatment groups.

2.22. *In vivo* biosafety assessment

After euthanasia, the hearts, livers, spleens, lungs, and kidneys of mice were harvested. These organs were fixed in a tissue fixative, embedded in paraffin, and sectioned. The sections were then stained with hematoxylin and eosin and photographed using a fluorescence microscope.

After 21 days of treatment, blood was collected from the eye sockets and allowed to stand at room temperature for a period of time. The supernatant serum was then collected by centrifugation (3000 rpm for 5 minutes). Serum biochemical parameters were then analyzed. Blood parameters measured included urea (UREA), lactate dehydrogenase (LDH), urea nitrogen (BUN), uric acid (UA), alkaline phosphatase (ALP), glucose (GLU), alanine aminotransferase (ALT), albumin (ALB), and aspartate aminotransferase (AST).

2.23. Statistical analysis

All data are presented as mean ± standard deviation. Differences between experimental groups were analyzed by one-way ANOVA using GraphPad Prism software (Inc., La Jolla, CA, USA). Significance was determined by P value, where $^*P < 0.05$, $^{**}P < 0.01$, $^{***}P < 0.001$ and $^{****}P < 0.0001$.

3. Results and discussion

3.1. Synthesis and characterization of Se@PDA@HA

Se NPs were grown on the PDA surface using an *in situ* reduction method to prevent aggregation.[25] TEM results showed that the Se@PDA nanoparticles were uniform, nearly spherical and had smooth surfaces (Fig. 1A). Elemental mapping revealed uniform distribution of C, O, and Se (Fig. 1B), indicating that Se was uniformly deposited on the PDA surface *via in situ* reduction, rather than simple adsorption or aggregation. DLS analysis further confirmed the excellent dispersion after stepwise assembly. The average particle sizes of PDA, Se@PDA, Se@PDA@CDDP, and Se@PDA@HA@CDDP were 193.9 ± 3.156 nm, 192.8 ± 2.444 nm, 198.8 ± 4.623 nm, and 174.8 ± 3.349 nm, respectively (Fig. 1C–F), with PDI values all below 0.35. HA coating slightly reduced the particle size, indicating a denser outer layer and significantly improved colloidal stability. The loading of selenium nanoparticles enhanced the negative charge on the PDA surface, contributing to improved dispersion stability and biocompatibility. After loading cisplatin onto Se@PDA, the potential increased, indicating that the cisplatin loading neutralized some of the surface negative charge. This change may be attributed to the coordination or electrostatic interaction between cations generated from cisplatin hydrolysis and the Se@PDA surface groups, thereby reducing the particle surface negative charge. Further coating with hyaluronic acid (HA) resulted in an additional increase in the particle's zeta potential. This change may stem from the polymeric shell formed by HA on the particle surface, shielding the core's negative charge, while the coating layer shifts the shear plane outward, leading to an increased measured potential. The abundant carboxyl groups in HA may also complex with cisplatin, further influencing the surface charge distribution (Fig. 1G). The XPS spectrum revealed characteristic peaks for C 1s, N 1s, O 1s, and Se 3d (Fig. 1H). The high-resolution Se 3d spectrum exhibited a typical doublet at ~54.28 eV (Fig. 1I), corresponding to elemental Se^0, indicating the potential redox activity of the generated Se.[26] As shown in Fig. 1J, due to the abundant hydroxyl groups in PDA, intermolecular hydrogen bonds were formed, resulting in an O–H stretching vibration at 3327 cm^{-1}. Further HA coating increased its intensity slightly, and the intensity of the C=O stretching vibration at 1655 cm^{-1} also increased slightly, demonstrating the effectiveness of the HA coating method.[27] UV-vis spectroscopy revealed enhanced absorption of Se@PDA@CDDP in the 250–280 nm range (Fig. 1K), demonstrating an overlapping pattern compared to free CDDP and Se@PDA, indicating that CDDP was effectively loaded into the carrier and

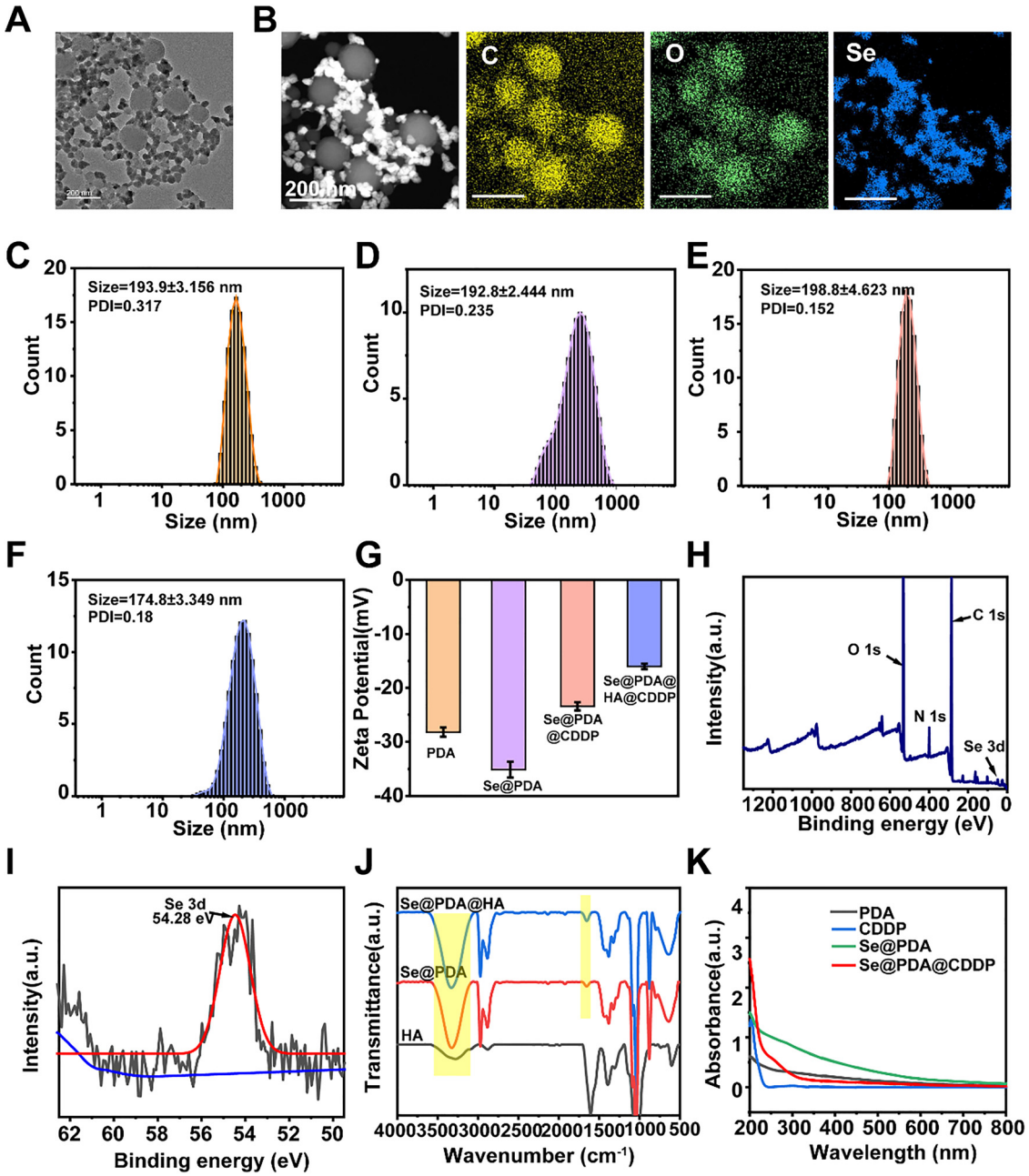

Fig. 1 (A) TEM image of Se@PDA. (B) Elemental mapping of Se@PDA. (C) Size distribution of PDA. (D) Size distribution of Se@PDA. (E) Size distribution of Se@PDA@CDDP. (F) Size distribution of Se@PDA@HA@CDDP. (G) Statistical histogram of Zeta potentials of different materials. (H) XPS full spectrum of Se@PDA. (I) XPS fine spectrum of Se 3d in Se@PDA. (J) FTIR images of HA, Se@PDA and Se@PDA@HA. (K) UV spectra of PDA, CDDP, Se@PDA, and Se@PDA@CDDP.

that HA coating did not compromise its structural integrity. Based on the linear regression equation for CDDP ($Y = 0.0217x + 0.0065$, $R^2 = 0.9991$), the drug loading efficiency was calculated to be 33.60%, and the encapsulation efficiency was 75.61%.

3.2. Photothermal properties and enzyme activity characterization of Se@PDA@HA@CDDP

In photothermal therapy, maintaining the local temperature at approximately 50 °C is generally regarded as an optimal therapeutic window, as it efficiently induces tumor cell apoptosis and necrosis while limiting collateral damage to surrounding normal tissues and simultaneously promoting immunogenic cell death and downstream antitumor immune activation. The photothermal behavior of Se@PDA nanoparticles was therefore systematically investigated under 808 nm laser irradiation. As shown in Fig. 2A, the temperature elevation of Se@PDA dispersions increased in a concentration-dependent manner. At a laser power density of 1.5 W cm^{-2} and a nanoparticle concentration of 100 μg mL^{-1}, the suspension

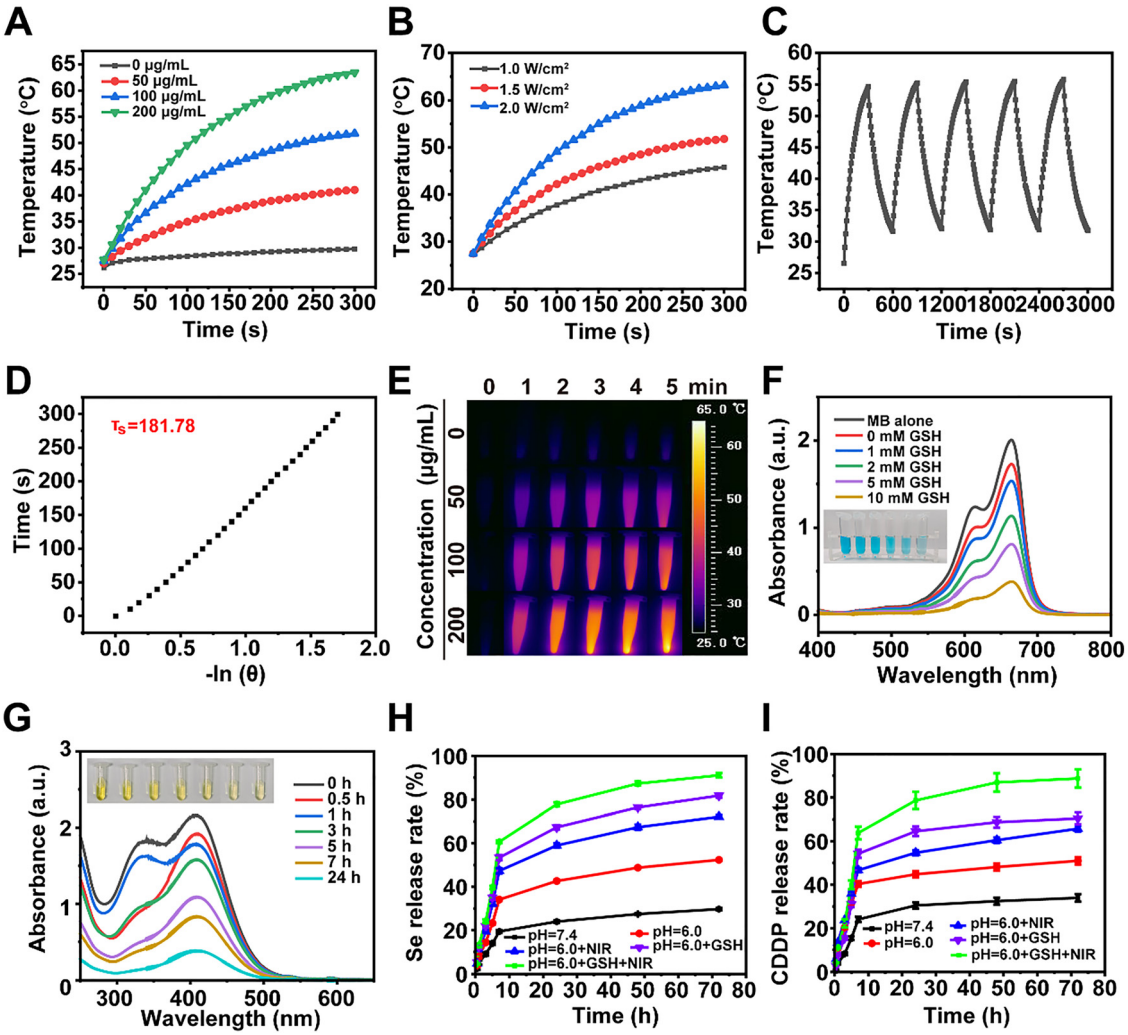

Fig. 2 (A) Heating curves of Se@PDA solutions with different concentrations at a laser power of 1.5 W cm^{-2}. (B) Temperature changes of Se@PDA solutions with a concentration of 100 μg mL^{-1} under laser irradiation at different power levels. (C) Temperature changes of Se@PDA solutions during continuous heating and cooling. (D) Photothermal time constant of Se@PDA solutions. (E) Infrared thermographic images of Se@PDA solutions with different concentrations as a function of time under laser irradiation at a power of 1.5 W cm^{-2}. (F) Detection of reactive oxygen species in Se@PDA. (G) Detection of GSH consumption in Se@PDA. Release diagrams of Se@PDA@CDDP: (H) CDDP release diagram and (I) Se release diagram.

was rapidly heated to 51.8 °C within 5 min, thereby entering the desired therapeutic range. When the nanoparticle concentration was kept constant at 100 μg mL^{-1}, higher laser power densities produced more pronounced temperature rises (Fig. 2B). Repeated heating–cooling cycles revealed nearly overlapping temperature profiles (Fig. 2C), indicating the excellent photothermal stability and recyclability of Se@PDA. On the basis of the linear fit of the cooling curves (Fig. 2D), the photothermal conversion efficiency was estimated to be ~54.28%, which surpasses that of most previously reported PDA-based photothermal agents. Infrared thermal imaging (Fig. 2E) further corroborated the strong and homogeneous photothermal response of Se@PDA under NIR irradiation. The reactive oxygen species (ROS) generation capacity of Se@PDA was then investigated using a methylene blue (MB) probe. Results (Fig. 2F) showed that the MB absorption peak intensity at 664 nm gradually decreased with increasing GSH concentration (0–10 mM), accompanied by a simultaneous color change (inset), indicating that Se@PDA reacts with GSH to form oxidative intermediates, thereby promoting ROS generation and exhibiting excellent redox activity.[28] Further GSH depletion experiments (Fig. 2G) revealed that the absorption intensity of the system decreased with increasing incubation time (0–24 h), indicating that Se@PDA can continuously deplete GSH through the Se–GSH cycle,[29] disrupting the intracellular antioxidant balance, thereby enhancing oxidative stress and synergizing tumor cell killing during chemotherapy. The drug release behavior of Se@PDA@CDDP nanoparticles under different conditions was also investigated. The release results (Fig. 2H and I) showed that after 72 hours, CDDP release reached 33.91% (pH 7.4), 50.98% (pH 6.0), 65.77% (pH 6.0 + NIR), 70.44% (pH 6.0 + GSH), and 88.75% (pH 6.0 + GSH + NIR). Since PDA readily decomposes under acidic conditions, leading to the release of Se NPs and CDDP, the Se ion release trend was

similar to that of CDDP, reaching 29.72% (pH 7.4), 52.39% (pH 6.0), 72.17% (pH 6.0 + NIR), 81.80% (pH 6.0 + GSH), and 91.15% (pH 6.0 + GSH + NIR) after 72 hours. The above results indicate that Se@PDA@CDDP has both pH/GSH dual sensitivity and photothermal response properties, which can achieve on-demand controllable release at the tumor site.

3.3. *In vitro* antitumor efficacy and mechanistic evaluation of Se@PDA@HA@CDDP nanoparticles

The cytotoxicity of Se@PDA@HA@CDDP nanoparticles toward L929 fibroblasts and their inhibitory effect on MC38 tumor cells were evaluated using the CCK-8 assay. As shown in Fig. 3A, after 24 h incubation with various concentrations of Se@PDA@HA@CDDP, no significant cytotoxicity was observed in L929 cells within the concentration range up to 200 μg mL^{-1}, indicating good biocompatibility. In contrast, MC38 cells showed a significant decrease in viability following Se@PDA@HA@CDDP treatment, with cell viability reduced to approximately 50% at 100 μg mL^{-1}, and further decreased under NIR irradiation, confirming the enhanced antitumor activity induced by photothermal synergy (Fig. 3B). To verify the targeting ability and cellular uptake behavior, flow cytometry was used to analyze the fluorescence intensity of MC38 cells incubated with Se@PDA@HA and non-HA-modified Se@PDA. As shown in Fig. 3C and D, fluorescence intensity increased with incubation time, and the HA-modified group displayed significantly stronger signals, demonstrating that HA functionalization promoted receptor-mediated endocytosis through CD44 interaction, thereby improving cellular internalization efficiency. Live/dead cell staining (Fig. 3E) further confirmed the therapeutic efficacy of different treatments. The control and control + NIR groups exhibited predominantly green fluorescence, indicating negligible cytotoxicity. Se@PDA@HA induced limited cell death, whereas Se@PDA@HA@CDDP caused extensive cell death. Notably, upon NIR irradiation, Se@PDA@HA@CDDP induced about 90% cell death, suggesting an excellent synergistic antitumor effect.

Apoptosis in MC38 cells, following the different treatments, was quantified by flow cytometry (Fig. 3F and G). While NIR irradiation alone did not induce measurable apoptosis, treatment with Se@PDA@HA@CDDP markedly enhanced cell death, yielding an apoptosis rate of approximately 38.77%. When NIR irradiation was incorporated, the apoptotic fraction further increased to 53.56%, underscoring the cooperative effect between chemotherapy and photothermal activation. Consistent with these findings, wound-healing assays (Fig. 3H and I) demonstrated that cells in the control and control + NIR groups readily migrated to close the scratch gap, whereas the drug-treated groups exhibited markedly attenuated migration behavior. Among all groups, Se@PDA@HA@CDDP combined with NIR irradiation produced the slowest wound closure and the fewest cells within the scratch region, indicating that the combined therapy most effectively suppressed tumor cell motility and metastatic potential.

Since mitochondria are central regulators of cellular energy metabolism and redox homeostasis, mitochondrial injury can amplify oxidative stress and contribute to therapy-induced cytotoxicity.[22,30] To assess mitochondrial function, JC-1 staining was employed to evaluate changes in the mitochondrial membrane potential ($\Delta\Psi_m$). As illustrated in Fig. 3J and K, untreated MC38 cells exhibited strong red fluorescence derived from JC-1 aggregates, indicative of intact $\Delta\Psi_m$. In contrast, Se@PDA@HA@CDDP-treated cells, particularly those receiving additional NIR irradiation, displayed a pronounced shift toward green fluorescence, reflecting mitochondrial depolarization and dysfunction triggered by the combined therapeutic regimen.

To further confirm ROS generation induced by photodynamic effects, intracellular ROS levels were measured using the DCFH-DA probe.[31] As shown in Fig. 3L and M, NIR irradiation alone did not increase ROS in MC38 cells, while Se@PDA@HA@CDDP + NIR treatment resulted in a marked enhancement of green fluorescence, demonstrating substantial ROS generation. Under acidic conditions, PDA degradation triggered the release of Se NPs and CDDP. The released Se NPs reacted with intracellular glutathione (GSH), leading to GSH depletion and ferroptosis-like cell death. As shown in Fig. 3N, GSH levels in cells treated with Se@PDA@HA@CDDP decreased significantly, and NIR irradiation further enhanced this depletion, likely due to ROS generation and subsequent oxidative damage, thus accelerating GSH consumption.

3.4. Se@PDA@HA@CDDP nanoparticles induce immunogenic cell death and repolarize macrophages toward the M1 phenotype

To verify whether Se@PDA@HA@CDDP treatment can trigger immunogenic cell death (ICD) and subsequently regulate macrophage polarization, we investigated ICD-related markers and immune activation signals in MC38 cells and RAW264.7 macrophages. As shown in Fig. 4A and B, after Se@PDA@HA@CDDP treatment, the expression of calreticulin (CRT), a well-known "phagocytic" signaling molecule on the cell membrane, was significantly increased, especially under near-infrared (NIR) irradiation.[32,33] The enhanced CRT translocation indicates that Se@PDA@HA@CDDP combined with NIR irradiation can effectively induce immunogenic cell death (ICD) in tumor cells, thereby promoting the recognition and phagocytosis of antigen-presenting cells. Similarly, immunofluorescence analysis of high-mobility group box 1 (HMGB1) (Fig. 4C and D) showed that HMGB1 was released in large quantities from the nucleus to the extracellular space in the Se@PDA@HA@CDDP, combined with the NIR irradiation group, further confirming the occurrence of ICD and the activation of immune stimulation pathways. Western blot analysis (Fig. 4E) showed that, compared with other groups, the expression level of phosphorylated NF-κB p65 (p-p65) was significantly increased after Se@PDA@HA@CDDP + NIR treatment (Fig. 4F). This result indicates that ROS accumulation and ICD induction may activate the NF-κB signaling pathway, which plays a crucial role in initiating immune responses and regulating macrophage polarization.[34] In comparison to traditional PDA@HA@CDDP systems, which primarily focus on drug delivery

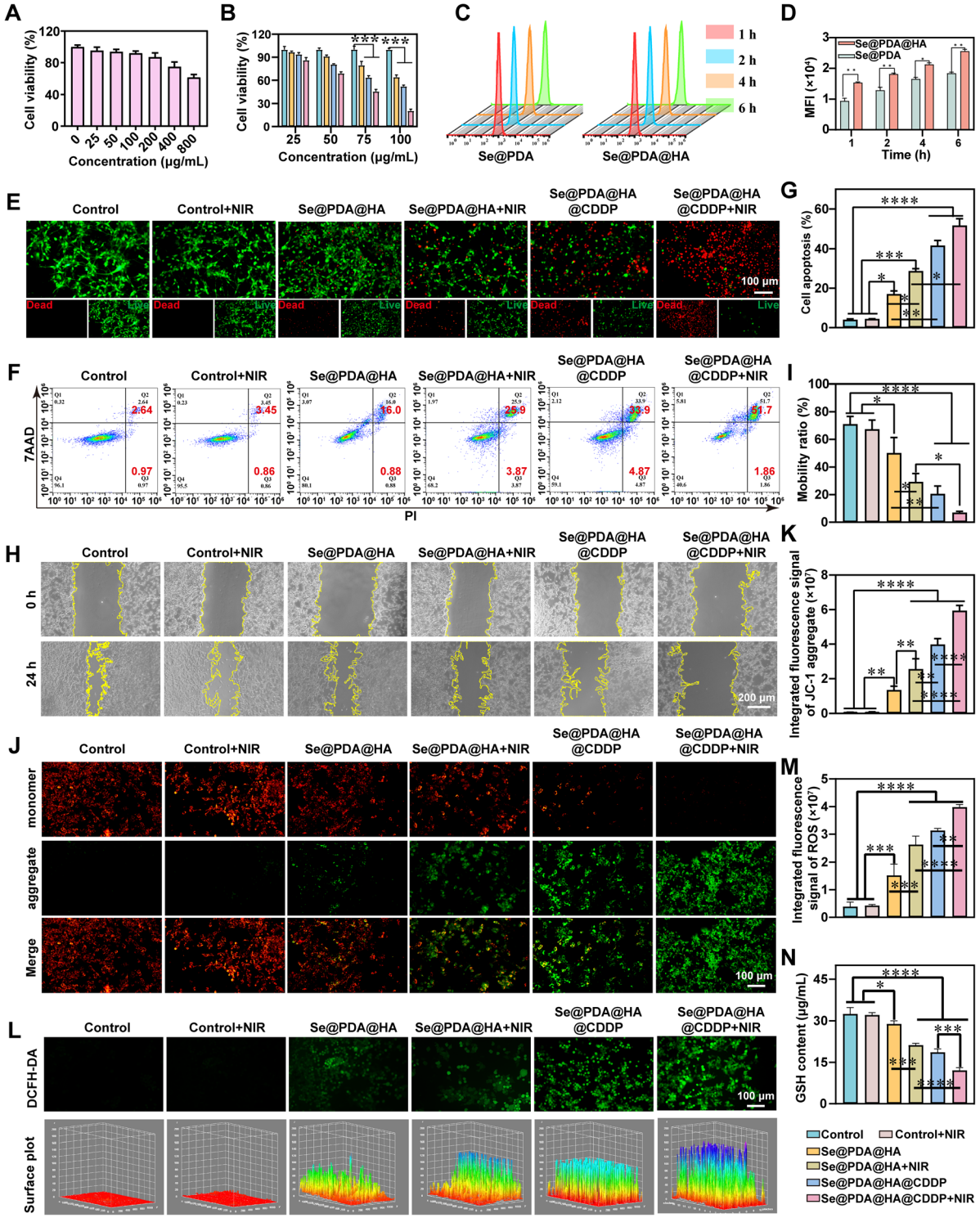

Fig. 3 (A) CCK-8 assay of L929 cells after incubation with different concentrations of Se@PDA@HA@CDDP for 24 hours. (B) CCK-8 assay of MC38 cells after incubation under different conditions for 24 hours. (C) and (D) Flow cytometry histograms and quantitative fluorescence data of MC38 cells incubated with Se@PDA@ICG or Se@PDA@HA @ICG for different time periods. (E) Live/dead staining of MC38 cells after treatment with different nanomaterials. Red fluorescence represents dead cells stained with propidium iodide (PI), and green fluorescence represents live cells stained with calcein (AM). (F) and (G) Apoptosis status and the corresponding apoptosis rates of MC38 cells treated with different nanomaterials. (H) and (I) Cell migration status and the corresponding migration rates of MC38 cells treated with different nanomaterials. (J) and (K) Fluorescence map of mitochondrial membrane potential in MC38 cells treated with different nanomaterials and the quantitative fluorescence of JC-1 aggregates in different groups. (L) and (M) Fluorescence map of intracellular ROS in MC38 cells treated with different nanomaterials and quantitative fluorescence of ROS. (N) Intracellular GSH content of MC38 cells treated with different nanomaterials.

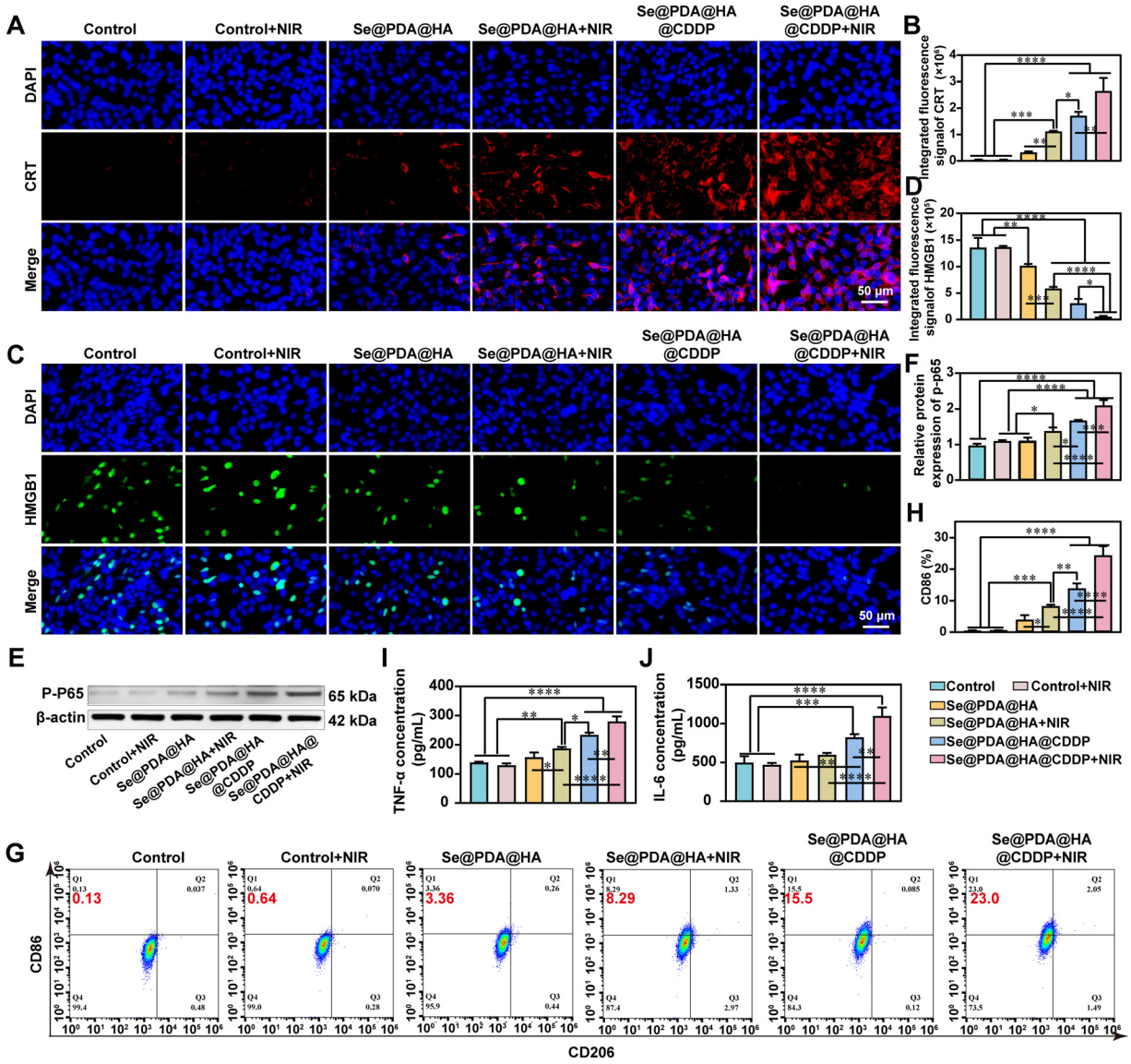

Fig. 4 (A) CRT exposure detection after MC38 cells were treated with different nanomaterials. (B) Mean fluorescence intensity of CRT. (C) Release of HMGB-1 after MC38 cells were treated with different nanomaterials. (D) Mean fluorescence intensity of HMGB-1. (E) Western blot analysis of MC38 cells after treatment with different nanomaterials. (F) Quantitative statistics of p-p65. (G) Polarized flow cytometry scatter plot of RAW264.7 cells after treatment with different nanomaterials. (H) Quantitative statistics of CD86 in different groups. (I) Statistical graph of TNF-α content in the RAW264.7 supernatant after treatment with different nanomaterials detected by ELISA. (J) Statistical graph of IL-6 content in the RAW264.7 supernatant after treatment with different nanomaterials, detected by ELISA.

and photothermal effects, our platform uniquely combines redox modulation and immune activation. By inducing immunogenic cell death (ICD) and activating NF-κB-dependent macrophage polarization, the Se@PDA@HA@CDDP platform also enhances systemic antitumor immunity, a feature that is not typically achieved by existing platforms.

To further verify the immunomodulatory effects induced by treatment, RAW264.7 macrophages were analyzed by flow cytometry to determine their phenotypic polarization status. As presented in Fig. 4G and H, exposure to Se@PDA@HA@CDDP combined with NIR irradiation resulted in a pronounced enrichment of $CD86^+$ macrophages, accompanied by a reduction in the $CD206^+$ population. This phenotypic redistribution reflects a transition from an M2 (immunosuppressive) state toward an M1 (pro-inflammatory) profile. Consistent with this observation, ELISA analysis of cytokine secretion (Fig. 4I and J) revealed markedly elevated concentrations of TNF-α and IL-6 in the culture supernatants of the Se@PDA@HA@CDDP + NIR group, further supporting the activation of pro-inflammatory macrophage subsets. Collectively, these findings indicate that Se@PDA@HA@CDDP nanoparticles, when stimulated by near-infrared irradiation, not only induce immunogenic tumor cell death but also facilitate activation of the NF-κB signaling pathway, thereby driving macrophage polarization toward an M1 phenotype. This dual-modality mechanism, integrating local tumor ablation with

immune priming, provides a mechanistic foundation for amplifying systemic antitumor immunity.

3.5. *In vivo* biodistribution and photothermal performance of Se@PDA@HA nanoparticles

To investigate the tumor-targeting ability and *in vivo* biodistribution of HA-modified nanoparticles, fluorescence imaging was performed using ICG-labeled Se@PDA nanoparticles. As shown in Fig. 5A, after intravenous injection, Se@PDA@HA@ICG exhibited a progressively enhanced fluorescence signal at the tumor site, reaching its peak intensity at approximately 3 h, whereas Se@PDA@ICG without HA modification mainly accumulated in the liver and spleen, showing only weak tumor localization. This result clearly demonstrates that HA modification significantly improves tumor accumulation through active targeting mediated by CD44 receptor recognition. *Ex vivo* fluorescence imaging of major organs and tumors at 8 h post-injection (Fig. 5B) further confirmed the preferential tumor accumulation of Se@PDA@ICG@HA. Quantitative analysis (Fig. 5C)

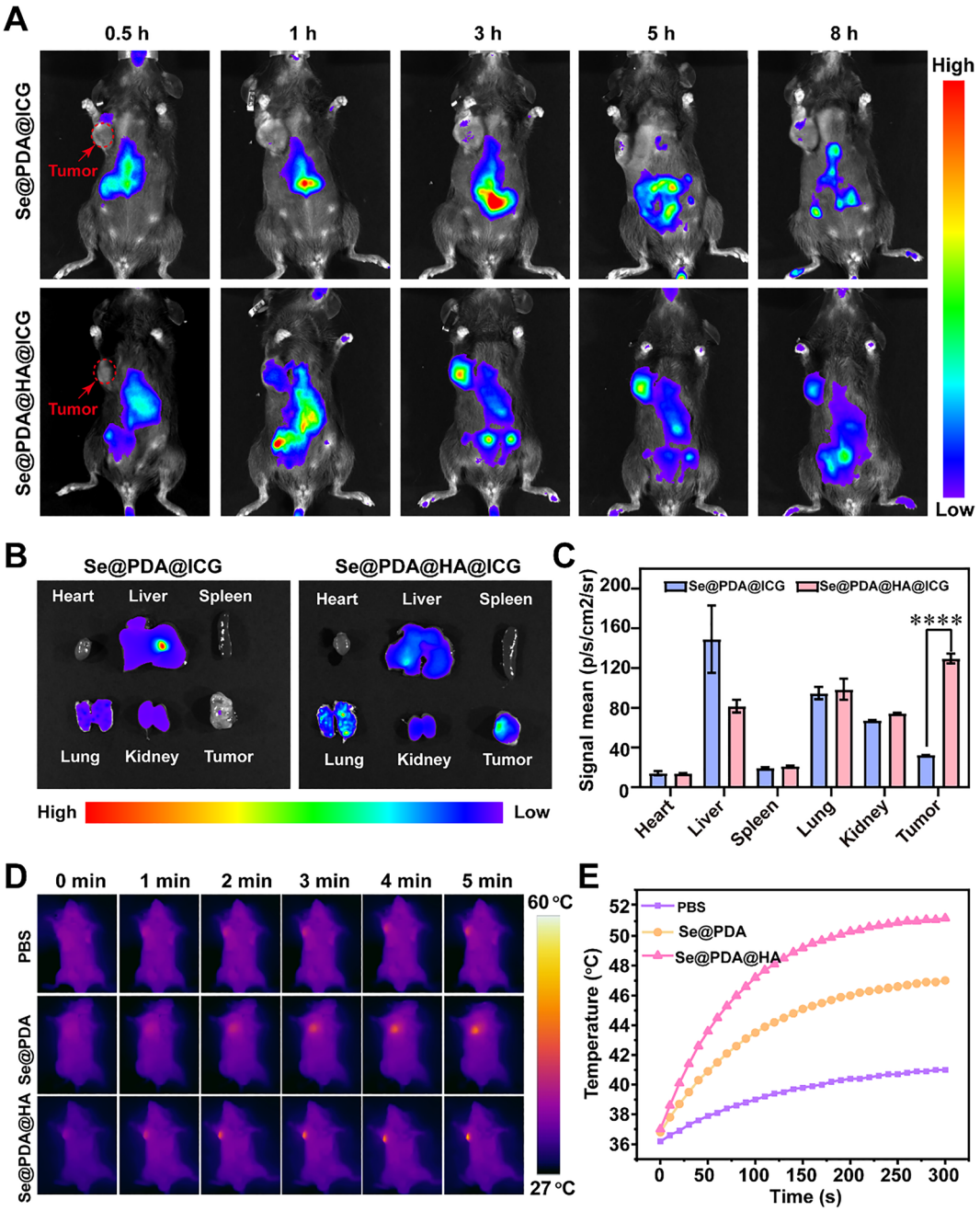

Fig. 5 (A) Fluorescence imaging of mice at different time points after intravenous injection of Se@PDA@ICG and Se@PDA@HA@ICG. (B) Fluorescence imaging of isolated organs of mice in different groups 8 hours later. (C) Quantitative fluorescence of isolated organs of mice in different groups. (D) Infrared thermographic images of mice after intravenous injection of PBS, Se@PDA and Se@PDA@HA after irradiation with 808 nm laser for different durations. (E) Temperature rise curves of mice in different groups after irradiation with 808 nm, 1.5 W cm^{-2} laser for 5 minutes.

showed that the fluorescence intensity in tumors treated with Se@PDA@HA@ICG was approximately 4-fold higher than that in the Se@PDA@ICG group, while fluorescence in the liver and spleen was relatively lower, indicating reduced reticuloendothelial system (RES) uptake and improved tumor-targeting efficiency.

The *in vivo* photothermal properties of Se@PDA@HA were further examined under NIR activation. Owing to the presence of hyaluronic acid on the nanoparticle surface, Se@PDA@HA exhibited enhanced affinity for CD44-overexpressing tumor cells, which markedly improved its tumor-homing capability following intravenous administration. As a result of this HA-mediated targeting, the intratumoral concentration of Se@PDA@HA was substantially higher than that of unmodified Se@PDA. This increased accumulation translated directly into superior photothermal behavior *in vivo*. As shown in Fig. 5D, NIR irradiation triggered a rapid temperature escalation at the tumor site in mice treated with Se@PDA@HA, with the temperature reaching ~50.7 °C within 5 min at a laser power density of 1.5 W cm^{-2}, which was sufficient to induce robust photothermal ablation. By comparison, Se@PDA produced only moderate heating, and PBS-treated animals exhibited no meaningful temperature change. The heating profiles in Fig. 5E corroborate these findings, demonstrating that Se@PDA@HA achieved the highest photothermal conversion efficiency among all the groups. This enhanced thermal response is consistent with its improved tumor accumulation and stronger optical absorption, both of which are derived from HA-mediated targeting.

3.6. *In vivo* antitumor efficacy of Se@PDA@HA@CDDP nanoparticles

The *in vivo* therapeutic performance of Se@PDA@HA@CDDP nanoparticles was evaluated in MC38 tumor-bearing mice under different treatment conditions. As shown in Fig. 6A, tumors in the PBS group displayed rapid and continuous growth, whereas free CDDP induced only moderate tumor inhibition. In contrast, Se@PDA@HA@CDDP nanoparticles markedly suppressed tumor growth, and the combination of Se@PDA@HA@CDDP with NIR irradiation produced the most pronounced antitumor effect, with the final tumor volume reduced to approximately 83.34% of that in the PBS control group. Quantitative analysis of tumor weights (Fig. 6B and C) further demonstrated that the Se@PDA@HA@CDDP + NIR group had the lowest tumor mass (0.13 g), indicative of a strong synergistic chemo–photothermal effect. Throughout the treatment period, mice receiving free CDDP exhibited a gradual decrease in body weight, reflecting the systemic toxicity associated with conventional cisplatin chemotherapy. By contrast, no significant body weight loss was observed in the Se@PDA@HA@CDDP or Se@PDA@HA@CDDP + NIR groups (Fig. 6D), suggesting negligible systemic toxicity and favorable biosafety of the nanoparticle formulation. Individual tumor growth curves (Fig. 6E) consistently showed that Se@PDA@HA@CDDP + NIR treatment led to near-complete suppression of tumor progression in all animals. Histological and immunofluorescence analyses further elucidated the underlying therapeutic mechanisms.

Hematoxylin and eosin (H&E) staining (Fig. 6F) revealed extensive necrosis in tumor tissues after Se@PDA@HA@CDDP + NIR treatment, whereas tumors in the PBS and CDDP groups maintained dense cellular structures. CD31 staining demonstrated markedly reduced microvessel density (Fig. 6G), indicating effective inhibition of tumor angiogenesis. Moreover, Ki67 staining (Fig. 6H) showed that the proliferation index was significantly decreased in the Se@PDA@HA@CDDP + NIR group compared to other treatments, confirming strong anti-proliferative activity. In contrast, TUNEL staining (Fig. 6I) exhibited extensive green fluorescence in the same group, representing widespread apoptotic cell death induced by the synergistic photothermal-chemotherapeutic effect. Taken together, these results demonstrate that Se@PDA@HA@CDDP nanoparticles, when combined with NIR irradiation, exert potent *in vivo* antitumor efficacy by inhibiting tumor proliferation and angiogenesis while inducing massive apoptosis, all with minimal systemic toxicity. This outcome highlights their promising potential as an integrated chemo-photothermal therapeutic platform for precise and effective cancer treatment.

3.7. Se@PDA@HA@CDDP nanoparticles promote dendritic cell maturation and enhance T cell immune activation

To clarify how Se@PDA@HA@CDDP modulates antitumor immunity *in vivo*, dendritic cell (DC) maturation and T-cell activation were assessed in tumor-draining lymph nodes (TDLNs) and tumor tissues from MC38-bearing mice following treatment. Flow cytometric profiling (Fig. 7A and B) demonstrated that combined Se@PDA@HA@CDDP + NIR treatment elicited a marked expansion of the mature DC population ($CD11c^+CD86^+$) in TDLNs. The proportion of mature DCs reached 32.36% in this group, representing a 2.3-fold increase relative to the PBS group. This robust enhancement of DC maturation indicates that the chemo-photothermal regimen substantially improves antigen-presenting capacity, in line with the occurrence of immunogenic cell death (ICD) triggered by the treatment. The promotion of DC maturation subsequently supports more efficient antigen processing and presentation, thereby priming the adaptive immune response. Activation of T cells within lymph nodes was further characterized to determine whether the increased antigen presentation translated into downstream immune activation. T cell activation in lymph nodes was further analyzed by detecting $CD3^+$, $CD4^+$, and $CD8^+$ subsets. As shown in Fig. 7C and D, the proportion of total $CD3^+$ T cells markedly increased in the Se@PDA@HA@CDDP + NIR group (53.7%) compared to the PBS and free CDDP groups (29.17% and 34.28%, respectively), suggesting enhanced T cell recruitment and activation. Moreover, flow cytometry results (Fig. 7E and G) demonstrated a significant rise in the proportion of cytotoxic $CD3^+CD8^+$ T cells (34.32%) and helper $CD3^+CD4^+$ T cells (27.16%) after Se@PDA@HA@CDDP + NIR treatment, confirming that this combinational therapy effectively stimulates both cellular and helper immune responses.

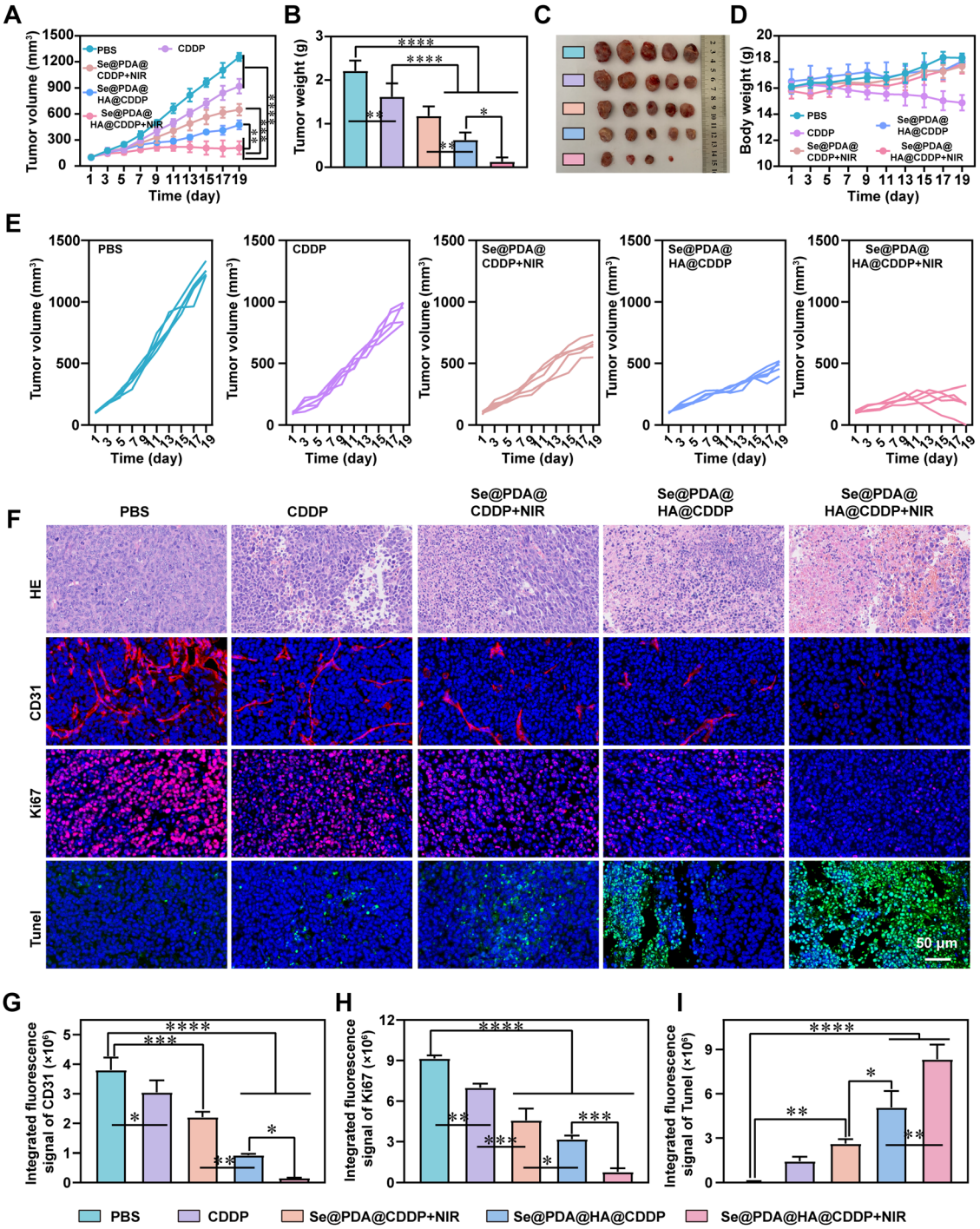

Fig. 6 Antitumor effects of Se@PDA@HA@CDDP *in vivo*. (A) Tumor volume curves of mice after different treatments. (B) Tumor weight of mice after different treatments. (C) Tumor images of mice after different treatments. (D) Body weight curves of mice after different treatments. (E) Tumor volume curves of mice in each group after different treatments. (F) HE, CD31, Ki67 and Tunel staining images of tumors in mice in different treatment groups. (G) Quantitative fluorescence of CD31 in tumors of mice in different treatment groups. (H) Quantitative fluorescence of Ki67 in tumors of mice in different treatment groups. (I) Quantitative fluorescence of Tunel in tumors of mice in different treatment groups.

Immunofluorescence staining of tumor sections (Fig. 7H) further supported these findings. The tumors from the PBS and CDDP groups showed sparse infiltration of T cells, whereas those treated with Se@PDA@HA@CDDP-especially with NIR irradiation, exhibited dense infiltration of $CD3^+$, $CD8^+$, and $CD4^+$ T cells. Quantitative analysis (Fig. 7I and K) revealed that fluorescence intensities corresponding to CD3, CD4, and CD8 were significantly higher in the Se@PDA@HA@CDDP + NIR group, suggesting robust intratumoral T cell activation and immune infiltration.[35] Collectively, Se@PDA@HA@CDDP

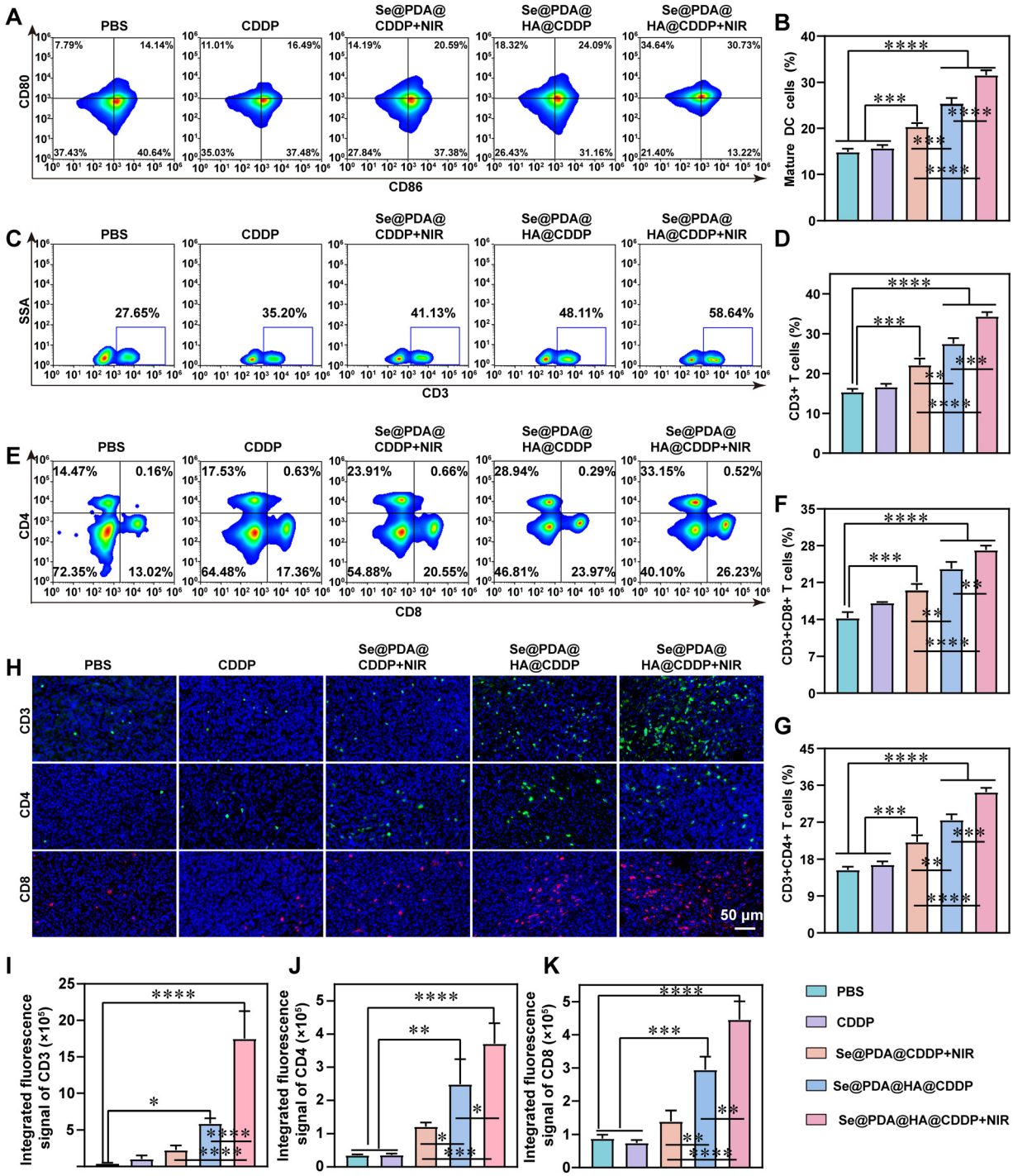

Fig. 7 (A) Flow cytometry analysis and quantification of mature dendritic cells (DCs) in lymph nodes of different groups. (B) and (C) Flow cytometry clustering and quantification of $CD3^+$ T cells in lymph node tissues of mice in each group. (D) and (E) Flow cytometry clustering of $CD3^+CD8^+$ T cells and $CD3^+CD4^+$ T cells in lymph node tissues of mice in each group. (F) Statistical bar chart of $CD3^+CD8^+$ T cells. (G) Statistical bar chart of $CD3^+CD4^+$ T cells. (H) Immunofluorescence sections of CD3, CD8, and CD4 in tumor tissues of mice in each group. (I) Quantitative fluorescence analysis of CD3 in tumor tissues of mice in each group. (J) Quantitative fluorescence analysis of CD4 in tumor tissues of mice in each group. (K) Quantitative fluorescence analysis of CD8 in tumor tissues of mice in each group.

nanoparticles, when combined with NIR irradiation, not only induce immunogenic cell death and dendritic cell maturation but also promote T cell activation and infiltration into tumor tissues. This immune activation cascade contributes to the establishment of a potent antitumor immune microenvironment, thereby enhancing systemic antitumor immunity and providing a promising strategy for synergistic chemo-photothermal-immunotherapy.

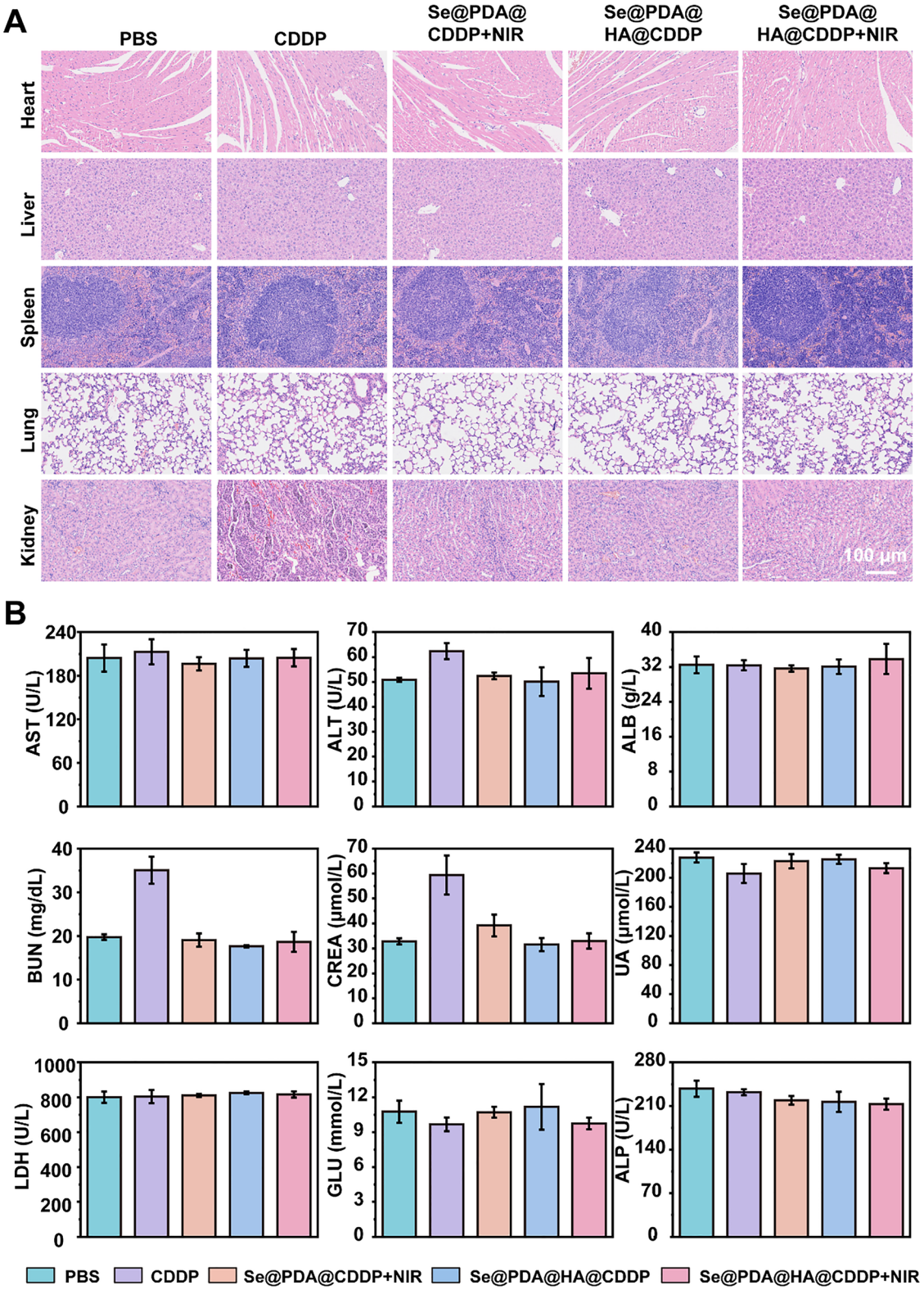

Fig. 8 *In vivo* safety verification. (A) H&E histological analysis of the major organs of mice in each group. (B) Analysis of serum biochemical indicators of mice in different experimental treatment groups (urea (UREA), lactate dehydrogenase (LDH), blood urea nitrogen (BUN), uric acid (UA), alkaline phosphatase (ALP), glucose (GLU), alanine aminotransferase (ALT), albumin (ALB), and aspartate aminotransferase (AST)).

Our Se@PDA@HA@CDDP platform significantly enhances these therapeutic outcomes by integrating four key mechanisms. First, the HA modification ensures CD44-mediated tumor-specific targeting, improving drug accumulation in tumor tissues and minimizing off-target effects. Second, the platform's pH/GSH-triggered drug release mechanism enables on-demand payload activation in the tumor microenvironment, further enhancing therapeutic efficiency. Third, the incorporation of selenium (Se) nanoparticles facilitates redox modulation, where Se consumption of GSH and ROS amplification promote oxidative stress, sensitizing tumor cells to chemotherapy. The addition of NIR-responsive photothermal therapy not only boosts drug release but also induces localized hyperthermic damage to tumor cells, synergizing with the chemotherapeutic effects.

3.8. *In vivo* biosafety assessment

To systematically evaluate the effects of different treatments on major organs in mice, H&E staining was performed on heart, liver, spleen, lung, and kidney tissues (Fig. 8A). No significant cell necrosis, inflammatory infiltration, or structural damage was observed in the PBS and Se@PDA@HA@CDDP + NIR groups; the tissue morphology remained intact, suggesting good tissue compatibility of the nanosystem and light treatment. In contrast, the free CDDP group showed mild tubular epithelial cell swelling, brush border degeneration, and focal vacuolar degeneration in the renal cortex.[36] These pathological features are consistent with cisplatin-induced acute kidney injury, indicating that free CDDP still exhibits dose-related nephrotoxicity *in vivo*.

Further analysis of serum biochemical indicators (Fig. 8B) showed that compared with the PBS control group, renal function indicators (UREA, BUN, and UA) in the free CDDP group showed an increasing trend, especially with significantly elevated BUN and UREA levels, indicating impaired renal tubular function.[37] Simultaneously, elevated lactate dehydrogenase (LDH) also reflected a certain degree of tissue damage. In both the Se@PDA@HA@CDDP and Se@PDA@HA@CDDP + NIR groups, renal function indicators remained within the normal range, significantly lower than in the free CDDP group. This indicates that the drug-loaded nanoplatform effectively avoided the non-specific distribution of free CDDP *in vivo* and reduced its typical nephrotoxicity. Liver function-related indicators (ALT, AST, ALP, and ALB) showed no significant fluctuations in any treatment group, indicating that the nanoformulation and photothermal assistance did not cause significant liver damage. Meanwhile, metabolic indicators such as glucose (GLU) remained stable.

The Se@PDA@HA@CDDP nanoplatform significantly reduced the typical nephrotoxicity caused by free CDDP, restoring both renal tissue pathology and renal function indicators to normal ranges. This improvement is mainly attributed to HA-mediated targeted enrichment and pH/GSH-responsive controlled release, which prevented high concentrations of CDDP accumulation in the kidneys, thereby improving overall biocompatibility.

4. Conclusion

This study presents a hyaluronic acid-modified pH/redox/near-infrared responsive nanoplatform (Se@PDA@HA@CDDP) that integrates targeted cisplatin delivery, selenium-driven redox regulation, and photothermal activation. Structural and physicochemical characterization confirmed that the nanoplatform possesses a uniform morphology, stable surface chemistry, efficient photothermal conversion, and glutathione-consuming/reactive oxygen species-amplifying activity, enabling on-demand drug release under tumor-like conditions. *In vitro* experiments showed that hyaluronic acid functionalization enhanced cellular uptake, and under near-infrared irradiation, the nanoplatform exhibited significant cytotoxicity, manifested as mitochondrial depolarization, apoptosis, reactive oxygen species burst, and glutathione depletion while remaining harmless to normal cells. Mechanistically, this therapy induces immunogenic cell death (CRT exposure and HMGB1 release) and activates NF-κB (p-p65), which collectively repolarize macrophages to the M1 phenotype and increase the expression of pro-inflammatory cytokines (TNF-α/IL-6). *In vivo* experiments showed that HA-guided tumor accumulation and excellent photothermal efficacy translated into significant tumor growth inhibition, reduced angiogenesis and proliferation, increased apoptosis, and strong immune activation (DC maturation; $CD3^+/CD8^+/CD4^+$ T cell infiltration). Histological and serum biochemical analyses indicated that it has good biocompatibility.

Author contributions

Yong Huang and Hong Hong were responsible for conceptualization, methodology, investigation, data curation, formal analysis and drafting of the manuscript. Lan Xia and Lifang Huang contributed to methodology, investigation and data curation. Chuqi Shao and Manli Qu assisted with investigation, validation and resource provision. Wenjun He and Suqiong Liang contributed to data analysis, visualization and critical revision of the manuscript. Cunchuan Wang and Yanping Qiu supervised the project, acquired funding, contributed to study conception and design, critically revised the manuscript, and served as corresponding authors.

Conflicts of interest

The authors declare no competing interests.

Data availability

The data supporting this article have been included as part of the supplementary information (SI). Supplementary information is available. See DOI: https://doi.org/10.1039/d5ma01372k.

Acknowledgements

The authors are grateful to all individuals and facilities that provided technical assistance and support during the completion of this study. This study was supported by the Science and

Technology Program for Social Development of Heyuan (Project Name: Early Screening Project for Colorectal Cancer in Heyuan; Project No. 230528211609112).

References

1 F. Bray, J. Ferlay, I. Soerjomataram, R. L. Siegel, L. A. Torre and A. Jemal, Global cancer statistics 2018: GLOBOCAN estimates of incidence and mortality worldwide for 36 cancers in 185 countries, *Ca-Cancer J. Clin.*, 2018, **68**(6), 394–424.

2 Z. Cheng, L. Huang, Y. Zhang, K. Yue, S. Jia, Z. Fang and Z. J. C. C. I. Lin, Heme oxygenase-1 leads to cisplatin resistance in nasopharyngeal carcinoma by reducing oxidative stress and ferroptosis, *Cancer Cell Int.*, 2025, **25**(1), 302.

3 R. Zhang, M. Chen, H. Zhou, Y. Liu, Y. Wang, C. Chen, Y. Li, J. Zeng, J. Cui and R. Duan, Eliminating Radioresistance With a Magnetic Ion-Generator by Simultaneously Augmenting DNA Damage and Diminishing Immunosuppression, *Adv. Mater.*, 2025, **37**(13), 2406378.

4 H. Ma, X. Li, X. Feng, Y. Li, D. Liu and L. Han, Mesoporous Silica-Based Nanomotors Loaded with Rapamycin for Synergistic Treatment of Rheumatoid Arthritis, *ACS Nano*, 2025, **19**(25), 22914–22930.

5 M. Sun, W. Liu, Y. Ma, P. Ni, W. Yao, Y. Xu, R. Bao, J. Wang, F. Xiong and X. Kuang, A photoswitchable phase-reversible gel engine for systemic redox homeostasis remodeling and on-demand chemodynamic immunotherapy with sustainable immunostimulation, *Chem. Eng. J.*, 2025, **507**, 160516.

6 Y. Zhang, Z. Fang, Z. Liu, K. Xi, Y. Zhang, D. Zhao, F. Feng, H. Geng, M. Liu and J. Lou, Implantable microneedle-mediated eradication of postoperative tumor foci mitigates glioblastoma relapse, *Adv. Mater.*, 2024, **36**(40), 2409857.

7 Y. Deng, Y. Gao, T. Li, S. Xiao, M. Adeli, R. D. Rodriguez, W. Geng, Q. Chen, C. Cheng and C. Zhao, Amorphizing metal selenides-based ROS biocatalysts at surface nanolayer toward ultrafast inflammatory diabetic wound healing, *ACS Nano*, 2023, **17**(3), 2943–2957.

8 C. E. Silva, A. S. Picco, F. E. Galdino, M. de Burgos Martins de Azevedo, M. Cathcarth, A. R. Passos and M. B. Cardoso, Distinguishing Protein Corona from Nanoparticle Aggregate Formation in Complex Biological Media Using X-ray Photon Correlation Spectroscopy, *Nano Lett.*, 2024, **24**(42), 13293–13299.

9 X. Li, C. Wu, J. Wu, R. Sun, B. Hou, C. Liu and M. Chen, Interfaces, Molecular investigation of the self-assembly mechanism underlying polydopamine coatings: the synergistic effect of typical building blocks acting on interfacial adhesion, *ACS Appl. Mater. Interfaces*, 2024, **16**(38), 51699–51714.

10 J. Li, W. Zhang, X. Luo, X. Wang, W. Deng, S. Wang, M. Zhao, Q. J. C. Zhao, S. A. Physicochemical and E. Aspects, A comparison between mesoporous and nonporous polydopamine as nanoplatforms for synergistic chemo-photothermal therapy, *Colloids Surf., A*, 2022, **653**, 130005.

11 X. Liu, N. Xu, X. Pu, J. Wang, X. Liao, Z. Huang and G. Yin, Combined photothermal-photodynamic therapy by indocyanine green loaded polydopamine nanoparticles enhances anti-mammary gland tumor efficacy, *J. Mater. Chem. B*, 2022, **10**(24), 4605–4614.

12 S. Kim, S. Li, A. K. Jangid, H. W. Park, D. J. Lee, H. S. Jung and K. Kim, Surface Engineering of Natural Killer Cells with CD44-targeting Ligands for Augmented Cancer Immunotherapy, *Small*, 2024, **20**(24), 2306738.

13 J. M. Espejo-Román, B. Rubio-Ruiz, V. Cano-Cortés, O. Cruz-López, S. Gonzalez-Resines, C. Domene, A. Conejo-García and R. M. Sánchez-Martín, Selective anticancer therapy based on a HA-CD44 interaction inhibitor loaded on polymeric nanoparticles, *Pharmaceutics*, 2022, **14**(4), 788.

14 C. Li, W. Jia, Z. Guo, Y. Kang, C. Zhou, R. Zhao, X. Cheng and N. Jia, A copper-platinum nanoplatform for synergistic photothermal and chemodynamic tumor therapy via ROS outburst and GSH exhaustion, *J. Mater. Chem. B*, 2024, **12**(3), 800–813.

15 J. Han, B. Wang, X. Zhao, C. Wang, D. Peng, Y. Liu, H. Zhu, W. Chen, Z. Cao and D. J. M. H. Wu, Host–guest supramolecular approach for the preparation of a 19 F MRI-guided theranostic agent with long T 2 relaxation times and its synergetic performances, *Mater. Horiz.*, 2025, 8577–8594.

16 R. Ding, H. Yang, J. Wang, Y. Liu, S. Mu, D. Wang and J. Li, Advances in Stimuli-Responsive Release Strategies for Sonosensitizers in Synergistic Sonodynamic Immunotherapy against Tumors, *Adv. Healthcare Mater.*, 2025, **14**(25), 2502183.

17 H. Wang, Y. Chen, R. Wei, J. Zhang, J. Zhu, W. Wang, Z. Wang, Z. Wupur, Y. Li and H. Meng, Synergistic Chemoimmunotherapy Augmentation via Sequential Nanocomposite Hydrogel-Mediated Reprogramming of Cancer-Associated Fibroblasts in Osteosarcoma, *Adv. Mater.*, 2024, **36**(15), 2309591.

18 Q. Xie, Y. Gao, W. Chen, H. Zhang, C. Fu, S. Batur, Y. Zhou, Y. Li, J. Zhang, Z. Zhang and L. Kong, Membrane fusogenic liposomes facilitate the production of immunostimulatory extracellular vesicles for enhanced cancer therapy, *J. Mater. Chem. B*, 2025, **13**(25), 7490–7501.

19 Y. Wang, G. Li, J. Su, Y. Liu, X. Zhang, G. Zhang, Z. Wu, J. Li, X. Wang and Y. Zhang, Tumor-Associated Macrophages Nano-Reprogrammers Induce ''Gear Effect'' to Empower Glioblastoma Immunotherapy, *Small*, 2025, **21**(6), 2406839.

20 P.-O. Gaudreau, M. V. Negrao, K. G. Mitchell, A. Reuben, E. M. Corsini, J. Li, T. V. Karpinets, Q. Wang, L. Diao and J. Wang, Neoadjuvant chemotherapy increases cytotoxic T cell, tissue resident memory T cell, and B cell infiltration in resectable NSCLC, *J. Thorac. Oncol.*, 2021, **16**(1), 127–139.

21 M. Amiri, O. Molavi, S. Sabetkam, S. Jafari and S. Montazersaheb, Stimulators of immunogenic cell death for cancer therapy: focusing on natural compounds, *Cancer Cell Int.*, 2023, **23**(1), 200.

22 J. Ren, Y. Hua, Z. Liao, X. Wen and Q. Wang, Subcellular two-pronged targeting therapeutics: disrupting mitochondria-endoplasmic reticulum communication in inflammatory disorders, *Acta Biomater.*, 2025, **208**, 95–118.

23 H. Chen, D. Wang, J. Liu, J. Chen, Y. Hu and Y. Ni, Interfaces, Augmenting Antitumor Immune Effects through the Coactivation of cGAS-STING and NF-κB Crosstalk in Dendritic Cells and Macrophages by Engineered Manganese Ferrite Nanohybrids, *ACS Appl. Mater. Interfaces*, 2025, **17**(9), 13375–13390.

24 Z. Malek-Esfandiari, A. Rezvani-Noghani, T. Sohrabi, P. Mokaberi, Z. Amiri-Tehranizadeh and J. Chamani, Molecular dynamics and multi-spectroscopic of the interaction behavior between bladder cancer cells and calf thymus DNA with rebeccamycin: apoptosis through the down regulation of PI3K/AKT signaling pathway, *J. Fluoresc.*, 2023, **33**(4), 1537–1557.

25 L. Wu, X. Bao, Z. Li, Y. Yu, Y. Liu, B. Xu, M. Zhou, Q. Wang and P. Wang, Rapid photothermal antibacterial and antifungal textiles through dynamic disulfide bond-assisted in-situ deposition of SeNPs, *Chem. Eng. J.*, 2024, **479**, 147772.

26 K. Chalastara and G. P. Demopoulos, Selenate Se (VI) reduction to elemental selenium on heterojunctioned rutile/brookite nano-photocatalysts with enhanced charge utilization, *Chem. Eng. J.*, 2022, **437**, 135470.

27 T. Mirzayeva, J. Čopíková, F. Kvasnička, R. Bleha and A. Synytsya, Screening of the chemical composition and identification of hyaluronic acid in food supplements by fractionation and Fourier-transform infrared spectroscopy, *Polymers*, 2021, **13**(22), 4002.

28 X. He, S. Rong and R. Zhang, Copper-doped melanin nanozyme with enhanced photothermal and peroxidase-like catalytic property for synergistic antimicrobial effect, *Mater. Lett.*, 2023, **341**, 134226.

29 R. Zhao, Y. Zhu, J. Zhou, B. Liu, Y. Du, S. Gai, R. Shen, L. Feng and P. Yang, Dual glutathione depletion enhanced enzyme catalytic activity for hyperthermia assisted tumor therapy on semi-metallic VSe2/Mn-CS, *ACS Nano*, 2022, **16**(7), 10904–10917.

30 J. Huang, L. Chen, Z.-M. Yao, X.-R. Sun, X.-H. Tong and S.-Y. Dong, Pharmacotherapy, The role of mitochondrial dynamics in cerebral ischemia-reperfusion injury, *Biomed. Pharmacother.*, 2023, **162**, 114671.

31 W. Wang, B. Ye, Y. Liu, Z. Li, Q. Huang, J. Zhou, M. Hu, J. Jiang, W. Wang, Z. Mao and Y. Ding, A long-term self-driven metronomic photodynamic system for cancer therapy, *Nat. Commun.*, 2025, **16**(1), 8823.

32 L. Xiao, L. Zhang, C. Guo, Q. Xin, X. Gu, C. Jiang and J. Wu, ''Find Me'' and ''Eat Me'' signals: tools to drive phagocytic processes for modulating antitumor immunity, *Cancer Commun.*, 2024, **44**(7), 791–832.

33 B. Chen, Y. He, L. Bai, S. Pan, Y. Wang, M. Mu, R. Fan, B. Han, P. E. Huber, B. Zou and G. Guo, Radiation-activated PD-L1 aptamer-functionalized nanoradiosensitizer to potentiate antitumor immunity in combined radioimmunotherapy and photothermal therapy, *J. Mater. Chem. B*, 2024, **12**(47), 12220–12231.

34 S. Wang, Y. He, J. Wang and E. J. B. Luo, Pharmacotherapy, Re-exploration of immunotherapy targeting EMT of hepatocellular carcinoma: Starting from the NF-κB pathway, *Biomed. Pharmacother.*, 2024, **174**, 116566.

35 A. I. Kraemer, C. Chong, F. Huber, H. Pak, B. J. Stevenson, M. Müller, J. Michaux, E. R. Altimiras, S. Rusakiewicz and L. Simó-Riudalbas, The immunopeptidome landscape associated with T cell infiltration, inflammation and immune editing in lung cancer, *Nat. Cancer*, 2023, **4**(5), 608–628.

36 Y. Wu, L. Zhao, L. Gu, A. Tilyek, B. Yu and C. Chai, Renoprotective activity of Ribes diacanthum pall (RDP) against inflammation in cisplatin-stimulated mice model and human renal tubular epithelial cells, *J. Ethnopharmacol.*, 2022, **283**, 114696.

37 Z. Zhao, K. He, B. Liu, W. Nie, X. Luo and J. Liu, Intrarenal pH-Responsive Self-Assembly of Luminescent Gold Nanoparticles for Diagnosis of Early Kidney Injury, *Angew. Chem., Int. Ed.*, 2024, **63**(29), e202406016.